






Flow Instabilities in Solar Jets in Their Upstream and Downstream Regimes

Xiaohong Li^{1,2} , Jun Zhang^{1,2}, Shuhong Yang^{1,2} , and Yijun Hou^{1,2} 

¹ CAS Key Laboratory of Solar Activity, National Astronomical Observatories, Chinese Academy of Sciences, Beijing 100101, People's Republic of China
lixiaohong@nao.cas.cn, zjun@nao.cas.cn

² School of Astronomy and Space Science, University of Chinese Academy of Sciences, Beijing 100049, People's Republic of China
Received 2018 October 8; revised 2019 February 27; accepted 2019 March 11; published 2019 April 16

Abstract

Using the Atmospheric Imaging Assembly 304 Å images obtained from the *Solar Dynamics Observatory*, we study two jets that occurred during the M5.8 class flare on 2017 April 3 and the M5.5 class flare on 2016 July 23, respectively. During the M5.8 class flare, many vortex-like structures occurred in the upstream and downstream regimes of the associated jet. While the jet was ejected upwards to the corona, some dark material at its base flowed through a bright structure with a velocity of 110 km s^{-1} . The boundary between the material and the structure changed from smooth to uneven. Later, the jet material at the higher atmosphere started to fall down with velocities of over 200 km s^{-1} , and the left boundary of the jet developed into a sawtooth pattern. The vortex-like structures were formed, and the growth rates of two structures were presented. During the M5.5 class flare, we also observed many vortex-like structures in the downstream regime of the jet. At the late stage of the jet, some material at the south boundary of the jet fell back to the solar surface, and vortex-like structures at the boundary grew from ripple-like minim into vortices with diameters of 3.4–5.4 Mm. The growth rates of the vortex-like structures were calculated. We suggest that the vortex-like structures in the upstream regime are the manifestations of Kelvin–Helmholtz instability, and those in the downstream regime are simultaneously driven by Kelvin–Helmholtz instability and Raleigh–Taylor instability.

Key words: Sun: activity – Sun: evolution – Sun: filaments, prominences – Sun: flares

Supporting material: animations

1. Introduction

Raleigh–Taylor instability (RTI) and Kelvin–Helmholtz instability (KHI) are basic instabilities in fluids and magnetized plasma. The RTI occurs at the interface between two fluids of different densities whenever fluids experience a pressure gradient that opposes the density gradient (Taylor 1950; Sharp 1984). The RTI is mostly gravitationally driven such as a dense fluid is supported against gravity above a lighter fluid. The influence of a magnetic field on the RTI depends on its component parallels to the interface, which can suppress the growth of the magnetic RTI through magnetic tension. Observations of the RTI include mushroom clouds from atmospheric nuclear explosions, supernova explosions in which expanding core gas is accelerated into denser interstellar medium (Wang & Chevalier 2001), and the finger-like structures in Crab Nebula (Hester et al. 1996).

The KHI arises at the interface of two parallel flows. In nonviscous fluids, the KHI will occur as long as there is a velocity shear. Since viscosity and magnetic field have stabilizing influences, a threshold of the velocity difference is required for the KHI to take place in magnetized plasma (Chandrasekhar 1961). In astrophysics and space physics, the KHI has been observed in many active phenomena, e.g., the solar wind (Suess et al. 2009), Earth's magnetopause (Hasegawa et al. 2004), planetary magnetotails (Masters et al. 2010), and cometary tails (Ershkovich 1980).

The solar atmosphere is made of hot and almost fully ionized plasma. The differences in densities and flow speeds between an expanse of erupting plasma and the background plasma may trigger the RTI and KHI. The RTI in the solar corona has been studied through the formation of plumes when a relatively dense solar prominence overlies a less dense plasma bubble

(Ryutova et al. 2010; Berger et al. 2011). The fragmentation of prominence eruption as the material falls back to the solar surface (Innes et al. 2012; Carlyle et al. 2014) and the filamentary structure associated with emerging magnetic flux (Isobe et al. 2005) are manifestations of the RTI as well. These observations are in accordance with the numerical simulations that in three-dimensions the RTI results in the formation of finger-like structures elongated in the direction of the magnetic field (Stone & Gardiner 2007). The KHI is also believed to operate in the solar atmosphere, with velocity difference exceeds twice the order of Alfvén velocity. The KHI can be identified by the appearance of growing ripples or the vortices that form across the boundary between two flows. Follon et al. (2011) observed the KHI in a fast coronal mass ejection (CME) event using the data taken by the *Solar Dynamics Observatory* (*SDO*; Pesnell et al. 2012). Ofman & Thompson (2011) confirmed the occurrence of the KHI in the solar corona, and the KHI in the solar prominence was also investigated by Berger et al. (2010) and Ryutova et al. (2010). Li et al. (2018) reported that the KHI developed at the boundary of a jet due to the strong velocity shear ($\sim 204 \text{ km s}^{-1}$) between two flows.

Solar jets, the plasma ejections along the open magnetic field lines in the solar corona, were discovered in the 1980s and then studied after the launch of the Japanese *Yohkon* satellite in the 1990s (Shibata et al. 1994; Shimojo et al. 1996). Subsequently, the unprecedented high-resolution observations by *Hinode* (Kosugi et al. 2007), *Solar TERrestrial Relations Observatory* (*STEREO*; Kaiser et al. 2008), *SDO*, and *Interface Region Imaging Spectrograph* (*IRIS*; De Pontieu et al. 2014) have made great improvements in our understanding of the solar jets (Savcheva et al. 2007; Shen et al. 2011; Tian et al. 2014). Solar jets have been observed all over the solar atmosphere including coronal holes (Yang et al. 2011b), quiet regions

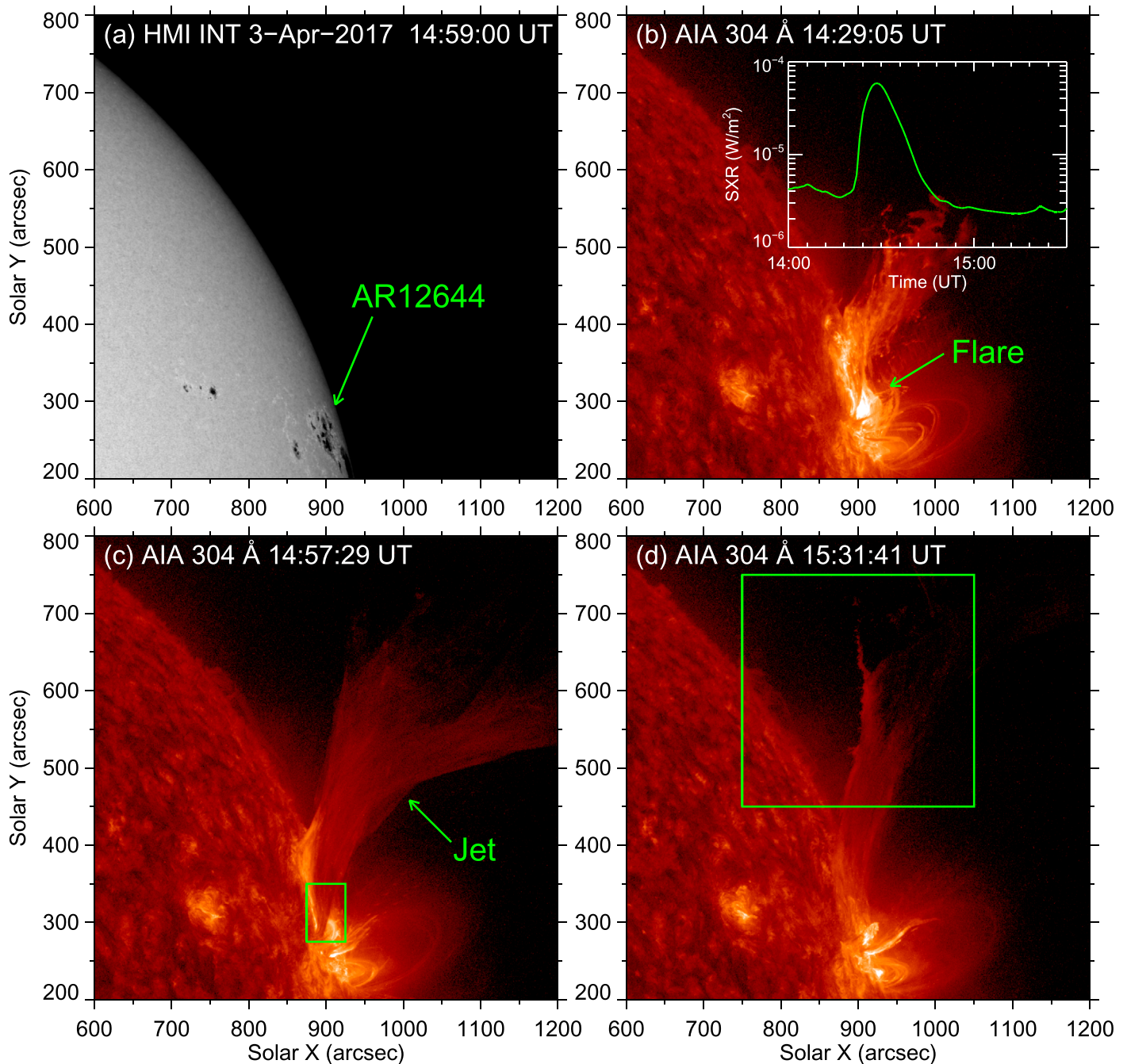


Figure 1. HMI continuum intensity (panel (a)) and AIA 304 Å images (panels (b)–(d)) displaying the overview of the jet on 2017 April 3. In panel (b), the green curve displays the variation of the *GOES* soft X-ray 1–8 Å flux. The green rectangle in panel (c) outlines the field of view (FOV) of Figure 2 and the green square in panel (d) outlines the FOV of Figure 3.

(Hong et al. 2011), and active regions (ARs; Li et al. 2015). Many wavelengths, e.g., X-ray (Sterling et al. 2015), extreme ultraviolet (EUV; Chae et al. 1999), and $H\alpha$ (Yokoyama & Shibata 1995) are employed to detect the jets. Coronal jets have apparent lengths of 10–400 Mm and widths of 5–100 Mm. The speeds of jets range from 10 to 1000 km s^{-1} , with a mean value of 200 km s^{-1} (Shimojo et al. 1996). The lifetimes of jets are 10–70 minutes, with a median value of 20–40 minutes (Nisticò et al. 2009). Jets have temperature in the range of 0.05 to 2.0 MK, while electron densities have been reported as 6.6×10^9 to $3.4 \times 10^{10} \text{ cm}^{-3}$ (Yang et al. 2011a). The magnetic field strength of the jets is a few Gauss (Pucci et al. 2013). The morphology, formation

mechanisms, and dynamic characters of the jets, as well as their relations to other coronal structures, have been carefully studied (Raouafi et al. 2016). However, studies of the instabilities in solar jets are still in early stages.

In this study, using the high-resolution data from the *SDO*, we present observations of the vortex-like structures in two solar jets. The first jet was located at AR 12644 and was associated with an M5.8 class flare on 2017 April 3. During this jet, we observed the vortex-like structures both in its upstream and downstream regimes, i.e., when the jet was ejected upwards to the corona and fell down from the higher atmosphere. We also observed the vortex-like structures driven

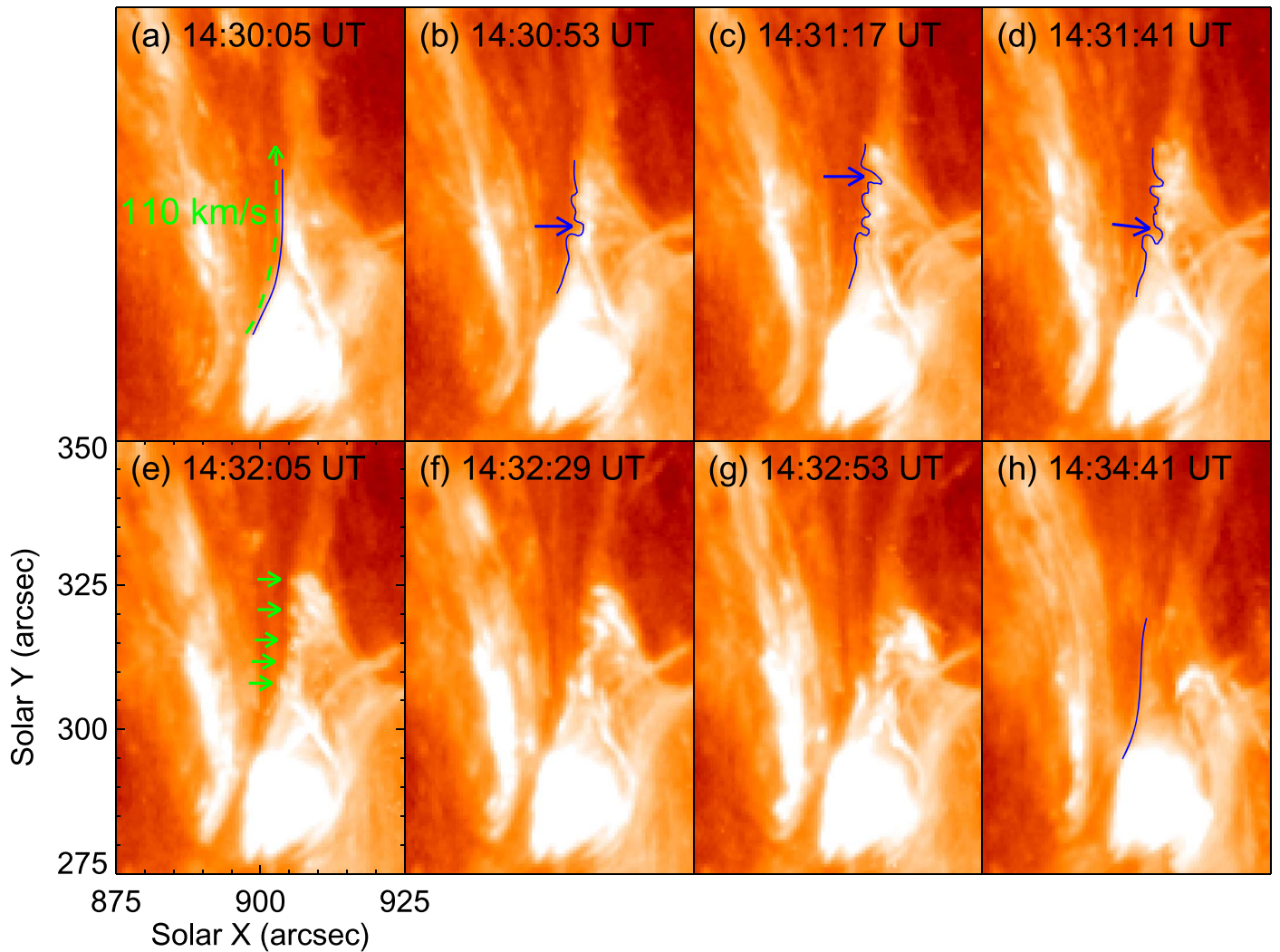


Figure 2. AIA 304 Å images showing the KHI in the upstream regime of the jet. The green dashed arrow in panel (a) displays the direction of the flow. In panels (a)–(d) and (h), the blue curves denote the left boundary of the jet. The green arrows in panel (e) point out five vortex-like structures caused by the KHI.

by the falling material of the jet during the M5.5 class flare on 2016 July 23. The vortex-like structures in the upstream regime of the jet are interpreted as evidence of the KHI, and the vortex-like structures in the downstream regime may be caused by both the RTI and KHI.

2. Observations and Data Analysis

We adopted the Atmospheric Imaging Assembly (AIA; Lemen et al. 2012) multiwavelength images and the Helioseismic and Magnetic Imager (HMI; Scherrer et al. 2012; Schou et al. 2012) data on board the *SDO*. For the M5.8 class flare on 2017 April 3, we chose the AIA 304 Å images, obtained from 14:00 UT to 16:00 UT with a pixel size of $0''.6$ and a cadence of 12 s. We also used the intensitygram from the HMI, with a spatial sampling of $0''.5 \text{ pixel}^{-1}$ and a 15 minute cadence, i.e., 1 frame in 20, from 2017 April 3 00:00 UT to 2017 April 4 00:00 UT. For the M5.5 class flare on 2016 July 23, we employed the AIA 304 Å images from 05:30 UT to 06:30 UT with a pixel size of $0''.6$ and a cadence of 12 s. In addition, we also employed the *Geostationary Operational Environmental Satellite* (*GOES*) data with the 1 minute cadence to examine the variation of soft X-ray 1–8 Å flux.

3. Results

On 2017 April 3, there were five ARs on the solar disk, and AR 12644, which we focus on, was located at the west boundary. At 14:19 UT, an M5.8 class flare took place in this AR. Associated with the M5.8 class flare, a jet occurred on the north side and its brief evolution is shown in Figure 1. The HMI intensitygram in panel (a) shows the location and appearance of the sunspot of AR 12644. The *GOES* soft X-ray 1–8 Å flux (see green curve in panel (b)) shows that the M5.8 class flare reached its peak at 14:29 UT, and the appearances of the flare and the jet at this moment are shown in panel (b). The jet took place at about 14:20 UT, and we observed numerous vortex-like structures during its evolution. The green rectangle in panel (c) and square in panel (d) display the positions where the vortex-like structures are observed, respectively.

Figure 2 shows the development of vortex-like structures that happened near the base of the jet. At 14:30 UT, the main mass of the jet was ejected outwards. At the base of the jet, some dark material flowed through the bright structure with a velocity of 110 km s^{-1} , and the boundary between the material and the structure was smooth as shown in panel (a). Then, the boundary

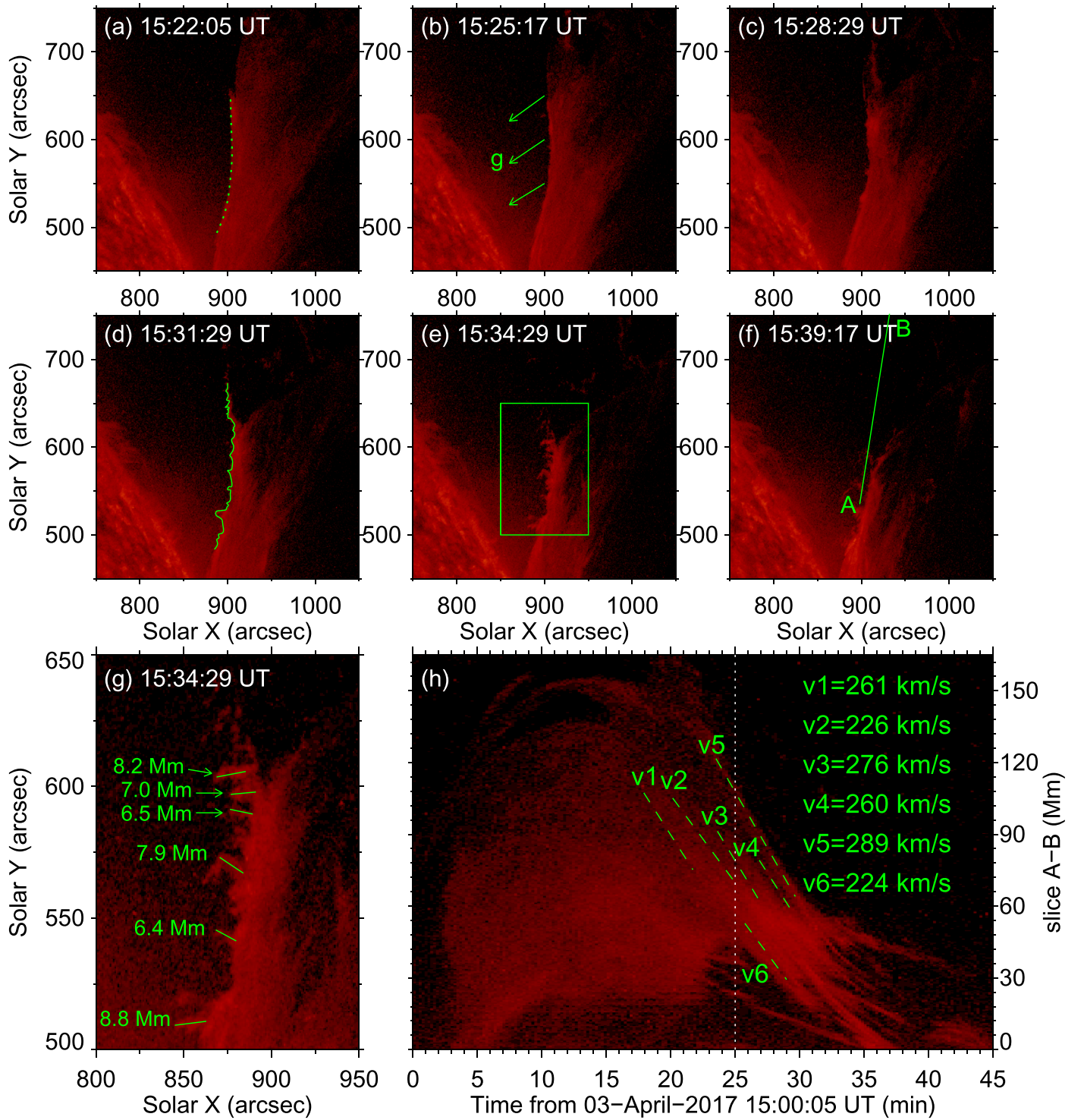


Figure 3. AIA 304 Å images (panels (a)–(f)) displaying the development of the vortex-like structures triggered by the falling material. The green curves in panels (a) and (d) denote the left boundary, which changes from being smooth into a sawtooth pattern. The green arrows in panel (b) display the directions of gravity at the points where arrows start. Panel (g) shows the expanded view of the area outlined by the green rectangle in panel (e), and the distortion values (6.4–8.8 Mm) of six vortex-like structures are marked. Panel (h) displays the space-time plot along the slice “A–B” as marked in panel (f). The velocities of selected representative bright structures are displayed. The white dotted line indicates the occurrence time of the vortex-like structures. The animation comprises unannotated AIA 304 Å images, running from 15:10 to 15:40 UT on 2017 April 3.

(An animation of this figure is available.)

became distorted as denoted by the blue curves in panels (b)–(d). The biggest distortion in each panel is indicated by the blue arrow, with a size scale of 1.7–2.5 Mm. The green arrows in panel (e) denote several vortex-like structures, and the

distance between two nearby structures is roughly 2.7–3.8 Mm. The vortex-like structures such as knots, growing ripples and so on are common phenomena in the solar atmosphere (Severny & Khokhlova 1953; Rothschild et al. 1955;

Sakurai 1976; Ofman & Thompson 2011). Some researchers interpreted the vortex-like structures appearing on the boundary between the jet and the ambient background as evidence of the KHI (Li et al. 2018; Zhelyazkov & Chandra 2018). Here, the velocity shear between the dark material and the bright structure drove the KHI, and the vortex-like structures were formed consequently. As the KHI developed, these structures became turbulent (see panels (f) and (g)). After the KHI, the boundary began smooth again as shown in panel (h).

Figure 3 and the animation show the evolution of the vortex-like structures at the left boundary of the jet. Due to the gravity, the jet material whose speed did not reach the escape speed started to drop at about 15:14 UT from the higher atmospheric layer. Along the left boundary of the jet (see slice “A–B” in panel (f)), we made a slice and the space-time plot is displayed in panel (h). We chose some trajectories and determined that the falling velocities of the jet material were approximately $224\text{--}289\text{ km s}^{-1}$. The left boundary of the jet was smooth initially, as shown in panel (a). At about 15:25 UT (see panel (b)), the boundary began to display ripple structures. These structures gradually developed and grew into vortex-like structures, which are displayed in panels (c) and (d). We chose some significant structures (see the green rectangle in panel (e)) when they were biggest and enlarged these structures in panel (g). The deformations were roughly 6.4–8.8 Mm. We chose two structures in panel (g) and measured their deformations over time. The deformations in three minutes are plotted in Figure 4. The deformations were exponential growths $d = d_0 e^{\gamma t}$, and the growth rates γ were estimated to be 0.0097 and 0.0088.

As the falling jet material was denser than the surrounding corona, and the interface was at some angle to gravity (the green arrows in Figure 3(b) display the directions of gravity at the points where the arrows start), these vortex-like structures in the downstream regime of the jet may be caused by the RTI. When magnetic field is not involved, the growth rate of the RTI is given as (e.g., Chandrasekhar 1961; Ryutova et al. 2010)

$$\gamma = \sqrt{(\rho_u - \rho_l)gk/(\rho_u + \rho_l)}, \quad (1)$$

where k is the wavenumber, g is the acceleration due to gravity, ρ_u is the upper density and ρ_l is the lower density (relative to the direction of gravity). We take the electron number density of the surrounding environment to be equal to $n_l = 10^{15}\text{ m}^{-3}$, and the electron number density of the jet is $n_u = 10^{16}\text{ m}^{-3}$, then the density can be derived as $\rho = n \cdot m$ ($m = 1.673 \times 10^{-27}\text{ kg}$). The solar gravitational acceleration is 273.2 m s^{-2} , then g is 236.6 m s^{-2} considering the angle between the gravity and the interface as 60° . The distance between two structures is regarded as the characteristic wavelength ($\sim 5000\text{ km}$). Thus, we can estimate that the growth rate is 0.0156 when the RTI is purely gravitationally driven. In solar jets, the magnetic field constrains the motion of the plasma. The inclusion of magnetic field adds a criterion for the occurrence of the RTI (Chandrasekhar 1961; Sharp 1984):

$$kg(\rho_u - \rho_l)/(\rho_u + \rho_l) > [(k \cdot \mathbf{B}_u)^2 + (k \cdot \mathbf{B}_l)^2]/\mu_0(\rho_u + \rho_l) \quad (2)$$

where \mathbf{B}_u and \mathbf{B}_l are the magnetic intensity of the upper and lower regions, respectively. Chen et al. (2012) assumed that the magnetic flux across the transverse section of the jet would

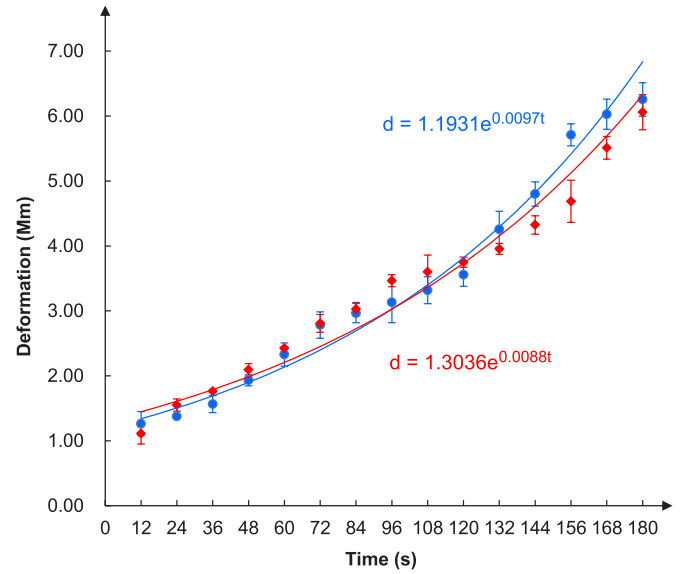


Figure 4. Growth rates of the vortex-like structures. We chose two structures in Figure 3(g) and measured their deformations over time five times. The blue and red points plot the average values and the error bars indicate the standard deviations. The blue and red curves denote corresponding fitted curves, and the fitted equations are displayed.

remain constant and found that the magnetic field inside the jet gradually decreases with the height from $15 \pm 4\text{ G}$ to about $3 \pm 1\text{ G}$ at a height of $7 \times 10^4\text{ km}$ ($\sim 100''$). Here, the heights where the vortex-like structures occurred were more than $100''$, so we assumed the magnetic field parallel to the interface to be $B_u = B_l = 3\text{ G}$. In consequence, the left term in Equation (2) is approximately 2.43×10^{-4} , and the right term is 1.23×10^{-2} , under which condition the RTI will not happen. As seen from the formula, the occurrence of the RTI would be influenced by the density and the magnetic field intensity. When the density of the jet ρ_u increases 10 times, the first term changes a little while the second term becomes approximately one-tenth of what it is now. So in a magnetohydrodynamic environment like corona, the RTI would happen when the density is high enough ($n > 10^{18}\text{ m}^{-3}$), that is the reason why so far very few case of filament eruption observed the RTI. When the magnetic field intensity becomes $B_u = B_l = 2\text{ G}$, the right term would change to four-ninths of the previous value ($\sim 5.5 \times 10^{-3}$). The density contrast of solar jets relative to background is not adequate for the RTI to develop, so other reasons may also contribute to the formation of the vortex-like structures. In our case, as there were velocity differences ($224\text{--}289\text{ km s}^{-1}$) between the dropping jet material and the ambient corona, the occurrence of the vortex-like structures may be driven by the KHI as well. When the gravity (the RTI) is not considered, the onset condition of the pure KHI in magnetized incompressible ideal plasma can be deduced by (Chandrasekhar 1961; Cowling 1976)

$$(\mathbf{k} \cdot \mathbf{V}_u - \mathbf{k} \cdot \mathbf{V}_l)^2 > (\rho_u + \rho_l) [(k \cdot \mathbf{B}_u)^2 + (k \cdot \mathbf{B}_l)^2]/\mu_0\rho_u\rho_l, \quad (3)$$

where \mathbf{k} , \mathbf{V} , \mathbf{B} , and ρ are the wave vector, velocity, magnetic field intensity, and mass density in the flux tube, respectively.

The subscripts “u” (“l”) indicate the quantities of the upper (lower) region. Presuming that $k\|\mathbf{V}_u\|\mathbf{V}_l\|\mathbf{B}_u\|\mathbf{B}_l$, then the velocity difference threshold is

$$\Delta V_s = |\mathbf{V}_u - \mathbf{V}_l| = \sqrt{(\rho_u + \rho_l)(B_u^2 + B_l^2)}/\mu_0\rho_u\rho_l. \quad (4)$$

Substituting the values into the formula, we can estimate that the velocity difference threshold is 307 km s^{-1} . When the magnetic field intensity decreases to $B_u = B_l = 2 \text{ G}$, the velocity difference threshold decreases to 205 km s^{-1} accordingly, and the KHI would happen. When the gravity is included, the instability would happen if (Chandrasekhar 1961)

$$\Delta V > \frac{\sqrt{(\rho_u + \rho_l)(B_u^2 + B_l^2)}/\mu_0\rho_u\rho_l - (\rho_u + \rho_l)(\rho_u - \rho_l)g/k\rho_u\rho_l}{\rho_u + \rho_l}. \quad (5)$$

If $\rho_u < \rho_l$, the second term beneath the radical sign will largen the velocity difference threshold, which means that the gravity with density gradient suppresses the KHI. If $\rho_u > \rho_l$, the second term will diminish the velocity difference threshold, which can be regarded as the manifestation of the RTI. Under our previous assumptions, the velocity difference threshold declines slightly (304 km s^{-1} when $B_u = B_l = 3 \text{ G}$ and 201 km s^{-1} when $B_u = B_l = 2 \text{ G}$), and the second term below the radical sign is roughly one-fiftieth of the first term, implying that the influence of the gravity may be very small. As the practical situation is complex, it is difficult to decide which instability is dominant. Hence, we interpret the occurrence of vortex-like structures as the result of both the RTI and the KHI. Under this circumstance, the growth rate (the imaginary part of frequency) can be deduced by (Guglielmi et al. 2010; Berger et al. 2017)

$$\gamma = \sqrt{kg(\rho_u - \rho_l)/(\rho_u + \rho_l) - k^2(B_u^2 + B_l^2)/\mu_0(\rho_u + \rho_l) + k^2\rho_u\rho_l(\Delta V)^2/(\rho_u + \rho_l)^2}. \quad (6)$$

The growth rate is sensitive to changes in magnetic field intensity. Choosing $\Delta V = 250 \text{ km s}^{-1}$, when $B_u = B_l = 3 \text{ G}$, the instability will not take place. When $B_u = B_l = 2 \text{ G}$, the growth rate is roughly 0.054, much higher than we estimated. Using the measured growth rate (~ 0.009), we can estimate that the magnetic field intensity is approximately 2.5 G ($B_u = B_l$), which is consistent with the actual magnetic field intensity of the jet and the corona (Chen et al. 2012).

We also observed the vortex-like structures caused by falling material in another jet that occurred on 2016 July 23. This jet took place in AR 12565, which was located on the west side of the solar disk. At 05:27 UT, an M5.5 class flare occurred, accompanying a large-scale jet (see Figure 5(a)). Massive plasma was ejected outwards. Later, some plasma fell back to the solar surface, and vortex-like structures developed at the south boundary of the jet as shown in panels (b1)–(b5) and the animation of Figure 5. The south boundary of the jet was smooth at first (see panel (b1)). At 05:48 UT, the boundary started to have ripple structures, which are indicated by the cyan arrows in panel (b2). The average distance between two adjacent structures was roughly 10 Mm. We studied the plasma movement at the positions of slices “A–B” and “C–D” (see

panel (b4)), and the temporal evolutions are displayed in Figures 6(a) and (b), respectively. At around 05:48 UT (see the vertical dashed lines in Figures 6(a) and (b)), the plasma at the south boundary of the jet started to fall back from the higher solar atmospheric layer. We chose several representative structures and measured their velocities, with values from 110 km s^{-1} to more than 270 km s^{-1} . Same as the last jet example, the gravity opposed the density gradient of the jet and the ambient corona, and was at some angle to their interface (see the green arrows in Figure 5(b2) which display the directions of gravity at the start points). Also, there existed velocity shear between the falling material and the ambient corona, so the vortex-like structures began to grow at the south boundary driven by both the RTI and the KHI. We chose three isolated structures (indicated by arrow “1” in Figure 5(b3) and arrows “2” and “3” in Figure 5(b5)), and their evolutions are presented in Figure 7.

Figure 7(a) is the space-time stack plot along the green enclosed area in Figure 5(b3) from 05:50 UT to 05:52 UT. The cadence of AIA 304 Å data is 12 s, so there are 10 images in two minutes. The blue arrows denote a vortex-like structure (indicated by arrow “1” in Figure 5(b3)), and its morphological changes and position movements are displayed. In the first image of panel (a), structure “1” looks like a ripple. Along with the development of the KHI over time, the structure grew and became a vortex-like structure. The diameter of structure “1,” marked by the cyan lines and arrows, is about 4.2 Mm in the last image of panel (a). Using the method displayed in Figure 4, we measured the changes of the vortex size (diameter) over time and determined the growth rate γ to be roughly 0.0087. Along the boundary of the jet, structure “1” moved approximately 21.8 Mm ($\sim 30''$) in two minutes, thus the velocity of structure “1” was about 181 km s^{-1} . Figure 7(b) is the space-time stack plot along the green enclosed area in

Figure 5(b3) from 06:02 UT to 06:06 UT with a cadence of 24 s. The white arrows indicate the vortex-like structure pointed out by arrow “2” in Figure 5(b5). In 168 s, structure “2” developed into a vortex-like structure with a diameter of 3.4 Mm (the cyan lines and arrows in the seventh image) and moved 21.0 Mm ($\sim 29''$), with the velocity of 125 km s^{-1} . The growth rate of structure “2” was estimated to be about 0.0070. There is another structure indicated by the green arrows in Figure 7(b) and arrow “3” in Figure 5(b5). This structure was tiny at first and grew to a clear vortex in the end, with the diameter of 5.4 Mm (see the cyan lines and arrows in the last image). The growth rate of structure “3” was approximately 0.0068. The position of structure “3” changed 32.6 Mm ($\sim 45''$) in four minutes, and the velocity of this structure was roughly 136 km s^{-1} . As demonstrated before, the growth rate can be estimated using Equation (6) when both the RTI and KHI are considered. Here, we use the same assumption that $B_u = B_l = 2 \text{ G}$, $n_u = 10^{16} \text{ m}^{-3}$, and $n_l = 10^{15} \text{ m}^{-3}$. The distance between two adjacent structures ($\sim 10 \text{ Mm}$) was regarded as wavelength. Considering the angle between the gravity and the interface as 45° and the velocity difference as $\Delta V = 200 \text{ km s}^{-1}$, then the growth rate is estimated to be 0.0057.

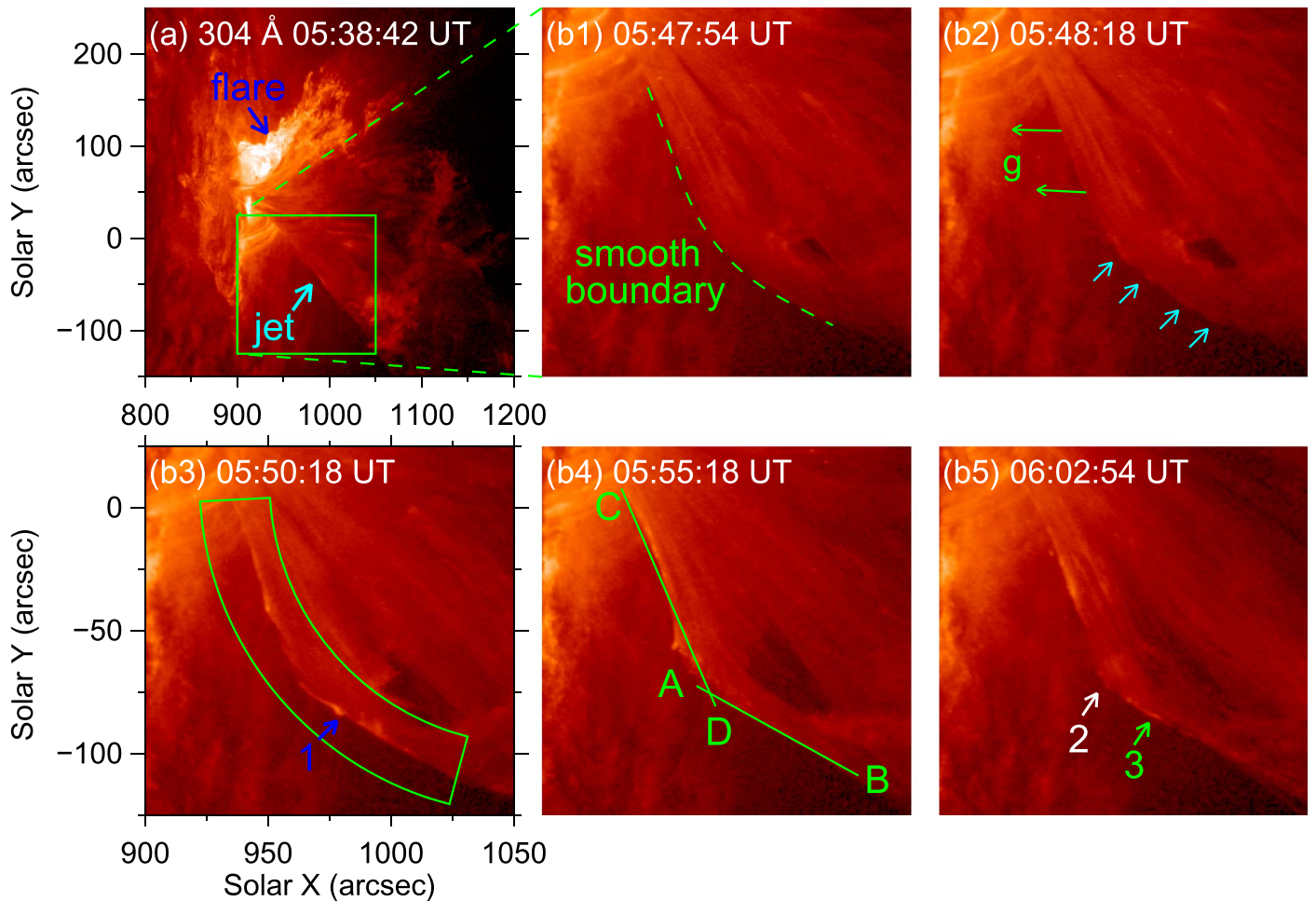


Figure 5. AIA 304 Å images displaying the vortex-like structures in the downstream regime of the jet on 2016 July 23. Panel (a): appearances of the M5.5 class flare and the jet. Panels (b1)–(b5): development of the vortex-like structures at the south boundary of the jet. The green arrows in panel (b2) display the directions of gravity at the points where arrows start. The cyan enclosed area in panel (b3) outlines the FOV of Figure 7. The numbered arrows in (b3) and (b5) indicate the structures that are displayed in Figure 7 with the same colors. In panel (b4), lines “A–B” and “C–D” display the cross-cut positions used to obtain the stack plots shown in Figure 6. The animation comprises unannotated AIA 304 Å images, running from 05:20 to 06:20 UT. (An animation of this figure is available.)

Remarkably, the measured values (0.0068–0.0087) are of the same order of the theoretically estimated values, implying that these vortex-like structures are simultaneously driven by the KHI and RTI.

4. Conclusions and Discussion

With the *SDO* observations, we studied the M5.8 class flare and the associated jet in AR 12644. Many vortex-like structures occurred during the development of the jet. As the jet material was ejected to the corona, dark material flowed through the bright structure at the base of the jet with velocity of 110 km s^{-1} , causing the KHI. The boundary between dark material and bright structure became distorted, and vortex-like structures grew with the biggest distortion of 1.7–2.5 Mm. Due to the gravity, the jet material whose speed did not reach the escape speed dropped down from the high atmospheric layer. The jet was denser and over 200 km s^{-1} faster than the ambient corona, thus the RTI and KHI occurred, and the boundary that was smooth at first started to display vortex-like structures with distortions of 6.4–8.8 Mm. We also studied the M5.5 class flare on 2016 July 23, and at the south boundary of the concomitant jet, the vortex-like structures also generated because of falling

material. The south boundary was smooth initially. Due to the density difference and velocity shear ($\sim 110 \text{ km s}^{-1}$ to more than 200 km s^{-1}) between the jet and the background, the RTI and KHI took place, and the boundary became distorted. We analyzed the evolution of the boundary, and found that there were small structures that grew from ripple-like minim into vortices whose diameters were roughly 3.4–5.4 Mm. The growth rates of the structures were approximately 0.0068–0.0087, and the downward velocities of these structures were over 100 km s^{-1} .

In the upstream regime of the jet, the vortex-like structures such as blobs appearing on the boundary between the jet and the corona have been reported before (Bogdanova et al. 2018; Li et al. 2018; Zhelyazkov & Chandra 2018), and they are interpreted as evidence of the KHI. The theory of the KHI in solar jets has been developed in recent years, and magneto-hydrodynamic (MHD) simulations support the presence of the KHI in solar jets (Zaqarashvili et al. 2015; Kuridze et al. 2016). Considering the distance between two structures (2.7–3.8 Mm) as wavelength ($\sim 3000 \text{ km}$), substituting the values $B_u = B_l = 3 \text{ G}$, $n_u = 10^{16} \text{ m}^{-3}$ and $n_l = 10^{15} \text{ m}^{-3}$ into Equation (5), we can estimate that the velocity difference

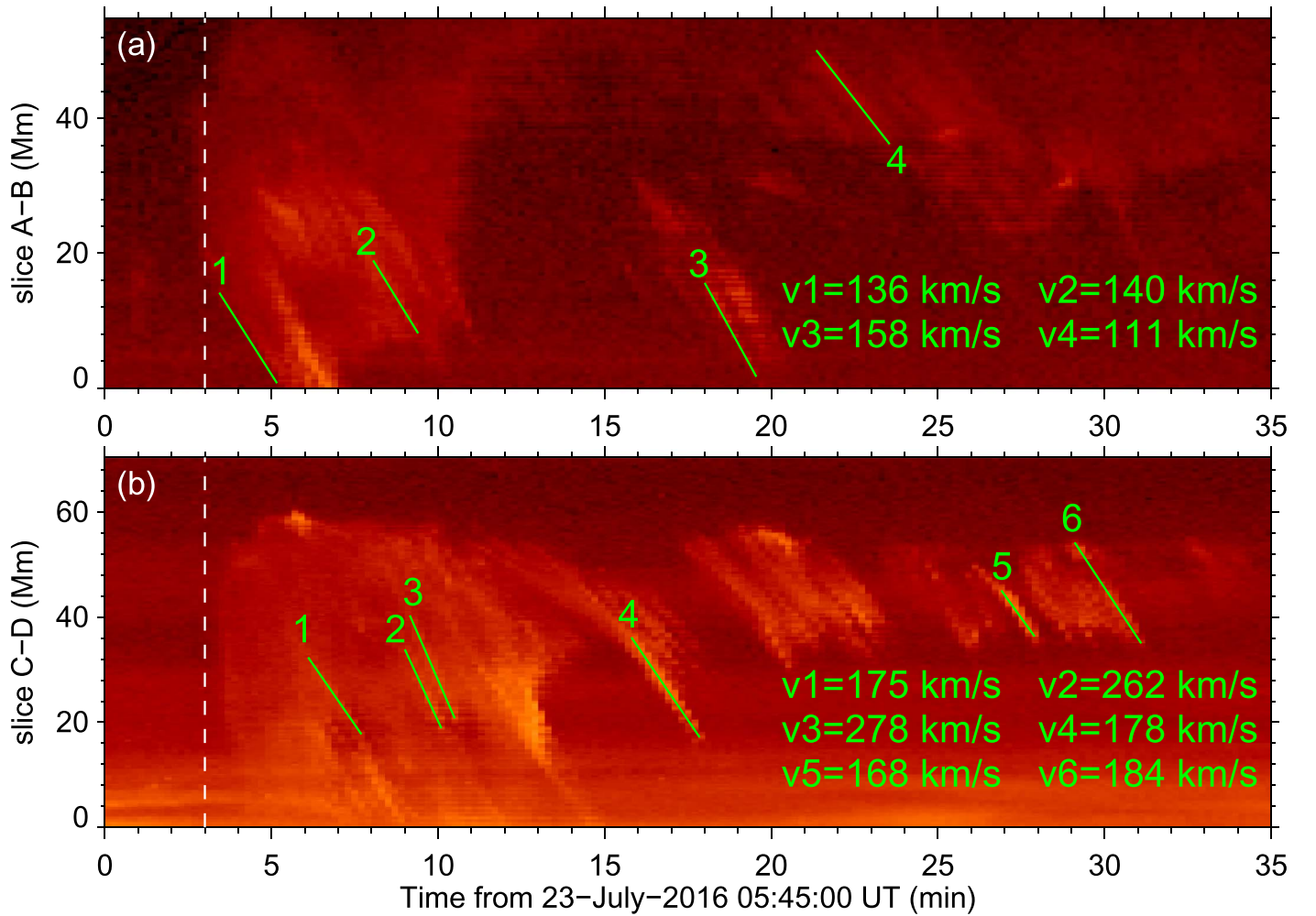


Figure 6. Temporal evolution at the positions of lines “A–B” and “C–D” in Figure 5(b4). The velocities of selected representative structures are displayed.

threshold of the KHI when the jet was ejected upwards was roughly 309 km s^{-1} , a little larger than the value when the gravity is not involved (307 km s^{-1}). Here, the KHI occurred when the velocity difference was 110 km s^{-1} , and there may be many reasons. First of all, the density of the bright structure may be larger than that of the corona. If we change the density of the bright structure to be $n_l = 10^{16} \text{ m}^{-3}$, then the velocity threshold becomes 131 km s^{-1} accordingly. From the results, we can see that density contrast has a huge impact on the onset of the KHI. Furthermore, the estimation is established under many preconditions, e.g., the plasma is incompressible, ideal, and $\mathbf{k} \parallel \mathbf{V}_u \parallel \mathbf{V}_l \parallel \mathbf{B}_u \parallel \mathbf{B}_l$, thus many parameters can influence the occurrence of the KHI besides the velocity and density contrast. As seen from Equation (3), the effect of a magnetic field on the KHI depends on both its intensity and orientation. Only magnetic field component parallels to the interface discontinuity can exert a restoring force and suppress the growth of the KHI, thus the magnetic field configurations of the jet and surrounding environment may affect the occurrence of KHI. Zhelyazkov et al. (2015) investigated the KHI in surges (cool jets) by modeling the surge as a moving twisted magnetic flux tube in homologous and twisted magnetic field. Their numerical studies showed that KHI occurred in magnetic field configurations for MHD waves propagating in axial direction, and the critical velocity for emerging KHI was remarkably lower ($24\text{--}60 \text{ km s}^{-1}$) when both magnetic fields were twisted.

Also, the compressibility of the plasma may change the instability criteria and growth rates (Sen 1964). Regarding EUV jets as a vertically moving flux tube (untwisted and weakly twisted), Zhelyazkov et al. (2016) found that the critical jet velocity was 112 km s^{-1} when the jet was assumed to be compressible plasma, and when the jet and its environment were treated as incompressible, the critical velocity became 114.8 km s^{-1} . Their work also proved that a weak twist of the magnetic field in the same approximation may decrease the threshold. Furthermore, viscosity may have a destabilizing influence when the viscosity coefficient takes different values at the two sides of the discontinuity, and therefore decrease the criteria of KHI (Ruderman et al. 1996). All these results reveal that the criteria of KHI can be reduced by many factors, and KHI can happen under the velocity difference of 110 km s^{-1} in the upstream regime of the jet.

Here, we also report the vortex-like structures that occurred when the jet material fell down, and these structures are interpreted as the result of the KHI and RTI. The coexistence of the RTI and KHI is not rare. In the nonlinear evolution of the RTI, the secondary KHI can be triggered as a result of the shear flows that develop between the falling material and the background (Cattaneo & Hughes 1988). Similarly, in the nonlinear evolution of the KHI, the rolled-up KH vortices would generate centrifugal force and create the conditions for the development of the RTI. In a more general case, there exist

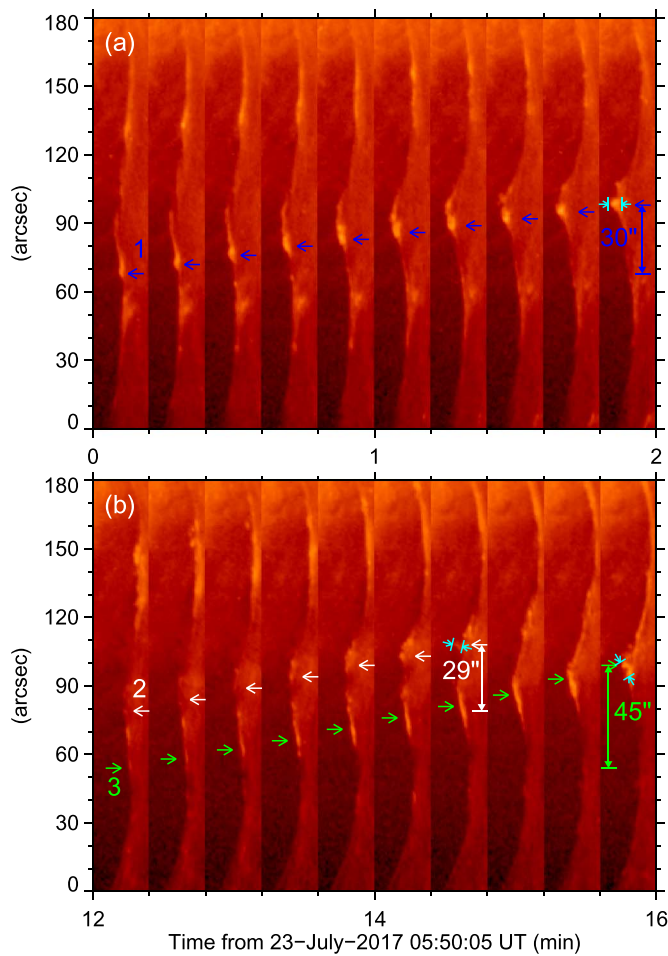


Figure 7. Development of the south boundary of the jet. The arrows with the same color denote the change of the location of the same vortex-like structure caused by the falling material. The diameter of each structure in the end is indicated by the cyan lines and arrows.

both the RTI and the KHI at the very beginning of a real system (Ye et al. 2011; Hillier 2018). In the downstream regime of the jet, the density and velocity differences between the jet material and the corona may trigger the RTI and KHI, as long as the stabilizing effect of the magnetic field are surpassed. Through theoretical analysis, the coaction of the RTI and the KHI in solar jets is proved, and there is little difference between the observed growth rates with the theoretical ones. The combination of the RTI and KHI has been studied before both theoretically and observationally, which is so-called coupled KH-RT instability or combined RT-KH instability (Farrugia et al. 1998; Berger et al. 2017). As we demonstrated before, there exist many preconditions in the derivation, and the occurrence of the KHI can be influenced by many factors. These factors such as the twisting of the magnetic field, the compressibility and viscosity of the fluids, and ion-neutral collisions would influence the RTI as well (Stone & Gardiner 2007; Liberatore et al. 2009; Díaz et al. 2012; Hillier 2016).

We thank the referee for valuable suggestions. This work is supported by the National Natural Science Foundations of China (11533008, 11790304, 11673035, 11773039, 11673034, 11790300), Key Programs of the Chinese Academy of Sciences (QYZDJ-SSW-SLH050), and the Youth Innovation Promotion

Association of CAS (2014043). The data are used courtesy of HMI, AIA, and GOES science teams.

ORCID iDs

Xiaohong Li <https://orcid.org/0000-0001-8164-5633>
 Shuhong Yang <https://orcid.org/0000-0002-6565-3251>
 Yijun Hou <https://orcid.org/0000-0002-9534-1638>

References

- Berger, T., Hillier, A., & Liu, W. 2017, *ApJ*, **850**, 60
 Berger, T., Slater, G., Hurlburt, N., et al. 2010, *ApJ*, **716**, 1288
 Berger, T., Testa, P., Hillier, A., et al. 2011, *Natur*, **472**, 197
 Bogdanova, M., Zhelyazkov, I., Joshi, R., & Chandra, R. 2018, *NewA*, **63**, 75
 Carlyle, J., Williams, D. R., van Driel-Gesztelyi, L., et al. 2014, *ApJ*, **782**, 87
 Cattaneo, F., & Hughes, D. W. 1988, *JFM*, **196**, 323
 Chae, J., Qiu, J., Wang, H., & Goode, P. R. 1999, *ApJL*, **513**, L75
 Chandrasekhar, S. 1961, International Series of Monographs on Physics (Oxford: Clarendon), 1961
 Chen, H.-D., Zhang, J., & Ma, S.-L. 2012, *RAA*, **12**, 573
 Cowling, T. G. 1976, Monographs on Astronomical Subjects (Bristol: Hilger), 1976
 De Pontieu, B., Title, A. M., Lemen, J. R., et al. 2014, *SoPh*, **289**, 2733
 Díaz, A. J., Soler, R., & Ballester, J. L. 2012, *ApJ*, **754**, 41
 Ershkovich, A. I. 1980, *SSRv*, **25**, 3
 Farrugia, C. J., Gratton, F. T., Bender, L., et al. 1998, *JGR*, **103**, 6703
 Foullon, C., Verwichte, E., Nakariakov, V. M., Nykyri, K., & Farrugia, C. J. 2011, *ApJL*, **729**, L8
 Guglielmi, A. V., Potapov, A. S., & Klain, B. I. 2010, *Ge&Ae*, **50**, 958
 Hasegawa, H., Fujimoto, M., Phan, T.-D., et al. 2004, *Natur*, **430**, 755
 Hester, J. J., Stone, J. M., Scowen, P. A., et al. 1996, *ApJ*, **456**, 225
 Hillier, A. 2018, *RvMPP*, **2**, 1
 Hillier, A. S. 2016, *MNRAS*, **462**, 2256
 Hong, J., Jiang, Y., Zheng, R., et al. 2011, *ApJL*, **738**, L20
 Innes, D. E., Cameron, R. H., Fletcher, L., Inhester, B., & Solanki, S. K. 2012, *A&A*, **540**, L10
 Isobe, H., Miyagoshi, T., Shibata, K., & Yokoyama, T. 2005, *Natur*, **434**, 478
 Kaiser, M. L., Kucera, T. A., Davila, J. M., et al. 2008, *SSRv*, **136**, 5
 Kosugi, T., Matsuzaki, K., Sakao, T., et al. 2007, *SoPh*, **243**, 3
 Kuridze, D., Zaqarashvili, T. V., Henriques, V., et al. 2016, *ApJ*, **830**, 133
 Lemen, J. R., Title, A. M., Akin, D. J., et al. 2012, *SoPh*, **275**, 17
 Li, X., Yang, S., Chen, H., Li, T., & Zhang, J. 2015, *ApJL*, **814**, L13
 Li, X., Zhang, J., Yang, S., Hou, Y., & Erdélyi, R. 2018, *NatSR*, **8**, 8136
 Liberatore, S., Jaouen, S., Tabakhoff, E., & Canaud, B. 2009, *PhPI*, **16**, 044502
 Masters, A., Achilleos, N., Kivelson, M. G., et al. 2010, *JGRA*, **115**, A07225
 Nisticò, G., Bothmer, V., Patsourakos, S., & Zimbardo, G. 2009, *SoPh*, **259**, 87
 Ofman, L., & Thompson, B. J. 2011, *ApJL*, **734**, L11
 Pesnell, W. D., Thompson, B. J., & Chamberlin, P. C. 2012, *SoPh*, **275**, 3
 Pucci, S., Poletto, G., Sterling, A. C., & Romoli, M. 2013, *ApJ*, **776**, 16
 Raouafi, N. E., Patsourakos, S., Parlat, E., et al. 2016, *SSRv*, **201**, 1
 Rothschild, K., Pecker, J.-C., & Roberts, W. O. 1955, *ApJ*, **121**, 224
 Ruderman, M. S., Verwichte, E., Erdélyi, R., & Goossens, M. 1996, *JPIPh*, **56**, 285
 Ryutova, M., Berger, T., Frank, Z., Tarbell, T., & Title, A. 2010, *SoPh*, **267**, 75
 Sakurai, T. 1976, *PASJ*, **28**, 177
 Savcheva, A., Cirtain, J., Deluca, E. E., et al. 2007, *PASJ*, **59**, S771
 Scherrer, P. H., Schou, J., Bush, R. I., et al. 2012, *SoPh*, **275**, 207
 Schou, J., Scherrer, P. H., Bush, R. I., et al. 2012, *SoPh*, **275**, 229
 Sen, A. K. 1964, *PhFI*, **7**, 1293
 Severny, A. B., & Khokhlova, V. L. 1953, *Izv. Krym. Astrofiz. Obs.*, **10**, 9
 Sharp, D. H. 1984, *PhyD*, **12**, 3
 Shen, Y., Liu, Y., Su, J., & Ibrahim, A. 2011, *ApJL*, **735**, L43
 Shibata, K., Nitta, N., Strong, K. T., et al. 1994, *ApJL*, **431**, L51
 Shimojo, M., Hashimoto, S., Shibata, K., et al. 1996, *PASJ*, **48**, 123
 Sterling, A. C., Moore, R. L., Falconer, D. A., & Adams, M. 2015, *Natur*, **523**, 437
 Stone, J. M., & Gardiner, T. 2007, *ApJ*, **671**, 1726
 Suess, S. T., Ko, Y.-K., von Steiger, R., & Moore, R. L. 2009, *JGRA*, **114**, A04103
 Taylor, G. 1950, *RSPSA*, **201**, 192
 Tian, H., DeLuca, E. E., Cranmer, S. R., et al. 2014, *Sci*, **346**, 1255711
 Wang, C.-Y., & Chevalier, R. A. 2001, *ApJ*, **549**, 1119
 Yang, L.-H., Jiang, Y.-C., Yang, J.-Y., et al. 2011a, *RAA*, **11**, 1229
 Yang, S., Zhang, J., Li, T., & Liu, Y. 2011b, *ApJL*, **732**, L7

Ye, W. H., Wang, L. F., Xue, C., Fan, Z. F., & He, X. T. 2011, *PhPI*, 18, 022704
Yokoyama, T., & Shibata, K. 1995, *Natur*, 375, 42
Zaqarashvili, T. V., Zhelyazkov, I., & Ofman, L. 2015, *ApJ*, 813, 123

Zhelyazkov, I., & Chandra, R. 2018, *MNRAS*, 478, 5505
Zhelyazkov, I., Chandra, R., & Srivastava, A. K. 2016, *Ap&SS*, 361, 51
Zhelyazkov, I., Zaqarashvili, T. V., Chandra, R., Srivastava, A. K., & Mishonov, T. 2015, *AdSpR*, 56, 2727